Die Grenzen der Chemie neu ausloten? It takes #HumanChemistry

Wir suchen kreative Chemikerinnen und Chemiker, die mit uns gemeinsam neue Wege gehen wollen – mit Fachwissen, Unternehmertum und Kreativität für innovative Lösungen. Informieren Sie sich unter:

evonik.de/karriere

EVONIK
Leading Beyond Chemistry

Check for updates

ADVANCED HEALTHCARE MATERIALS
www.advhealthmat.de

Biocompatible Micron-Scale Silk Fibers Fabricated by Microfluidic Wet Spinning

*Arne Lüken, Matthias Geiger, Lea Steinbeck, Anna-Christin Joel, Angelika Lampert, John Linkhorst, and Matthias Wessling**

For successful material deployment in tissue engineering, the material itself, its mechanical properties, and the microscopic geometry of the product are of particular interest. While silk is a widely applied protein-based tissue engineering material with strong mechanical properties, the size and shape of artificially spun silk fibers are limited by existing processes. This study adjusts a microfluidic spinneret to manufacture micron-sized wet-spun fibers with three different materials enabling diverse geometries for tissue engineering applications. The spinneret is direct laser written (DLW) inside a microfluidic polydimethylsiloxane (PDMS) chip using two-photon lithography, applying a novel surface treatment that enables a tight print-channel sealing. Alginate, polyacrylonitrile, and silk fibers with diameters down to 1 µm are spun, while the spinneret geometry controls the shape of the silk fiber, and the spinning process tailors the mechanical property. Cell-cultivation experiments affirm bio-compatibility and showcase an interplay between the cell-sized fibers and cells. The presented spinning process pushes the boundaries of fiber fabrication toward smaller diameters and more complex shapes with increased surface-to-volume ratio and will substantially contribute to future tailored tissue engineering materials for healthcare applications.

1. Introduction

Fiber-based tissue engineering has great potential in medical applications such as muscle repair, tendon replacement, and even nerve regeneration. In contrast to growing tissues on flat surfaces, such as well-plates, fibrous scaffolds support cells in a 3D environment more similar to the natural extracellular matrix, allowing them to migrate, grow, and proliferate.[1–4] Anisotropic tissue types, such as muscle or nerve tissue, require cell orientation and organization. In aligned fibrous scaffolds, the fiber's intrinsic anisotropy guides and directs cell growth toward alignment.[5–7] Here, the fiber's diameter and surface morphology are crucial.[8,9]

Hwang et al.[3] show that a decrease in fiber diameter from 150 to 12 µm significantly improves the alignment of neuronal cells along the fiber axis. Similarly, Kang et al.[10] report that fibers with longitudinal grooves with widths ranging from 2 to 10 µm improve alignment and directed growth of cells, compared to unstructured fibers. For optimal cultivation of cells, it is desirable to produce fibers with diameters in the single-digit micrometer range. Not only the fiber's diameter but also its material is crucial for cell survival. Materials for fibrous scaffolds need to be biocompatible and non-cytotoxic. A tailored material environment can direct growth and guide stem-cell differentiation.[11] Despite intense research, the production of fibers with tailored diameters and mechanical and material properties suitable for cell culture remains challenging.[1,4,12]

On an industrial scale, fibers are typically produced via a melt-extrusion process (dry-spinning) or spinning into a precipitation bath (wet-spinning). Both techniques are scalable and well suited for producing fibers with diameters larger than 100 µm, too large for tissue engineering scaffolds. Smaller fibers with single micron diameters are fabricated on a lab scale using electrospinning and microfluidic spinning. In electrospinning, a polymer is either molten or dissolved in a volatile solvent to create a homogeneous spinning dope. By applying a high voltage, the spinning dope is stretched into thin jets. Due to freezing or solvent evaporation, the jets solidify, leaving fibers with diameters as low as 100 nm.[13–15] The fibers deposit as an unordered non-woven on a collecting electrode, making it challenging to obtain oriented or individual fibers. Thus, electrospinning is not easily applicable

A. Lüken, M. Geiger, L. Steinbeck, J. Linkhorst, M. Wessling
Chemical Process Engineering
RWTH Aachen University
Forckenbeckstr. 51, Aachen 52074, Germany
E-mail: manuscripts.cvt@avt.rwth-aachen.de
A.-C. Joel
Institute of Biology II
RWTH Aachen University
Worringerweg 3, Aachen 52074, Germany
A. Lampert
Institute of Physiology
Uniklinik RWTH Aachen University
Pauwelsstraße 30, Aachen 52074, Germany
M. Wessling
DWI - Leibniz Institute for Interactive Materials
Forckenbeckstr. 50, Aachen 52074, Germany

The ORCID identification number(s) for the author(s) of this article can be found under https://doi.org/10.1002/adhm.202100898

© 2021 The Authors. Advanced Healthcare Materials published by Wiley-VCH GmbH. This is an open access article under the terms of the Creative Commons Attribution-NonCommercial-NoDerivs License, which permits use and distribution in any medium, provided the original work is properly cited, the use is non-commercial and no modifications or adaptations are made.

DOI: 10.1002/adhm.202100898

for the production of anisotropic tissue engineering scaffolds. Additionally, the preparation of suitable spinning dopes restricts the material selection. Delicate biological materials, such as proteins, get damaged by the high voltages.

Microfluidic spinning utilizes flow-focusing geometries in the jetting regime to produce stable, concentric co-flows of pre-polymer and shear fluid. The pre-polymer solidifies to form a fiber. s, solidifying to a fiber. The surrounding fluid prevents contact of the solidified polymer to the channel walls, avoiding adhesion, and thus reduces clogging.[12,16] Microfluidic spinning is, for the most part, realized with two types of devices. One type utilizes planar flow-focusing junctions produced from PDMS via soft-lithography for hydrodynamic focusing; the other achieves coaxial flow-focusing via devices assembled from glass micro-capillaries. In microfluidic flow-focusing junctions, the spinning dope is focused laterally by a shear fluid entering through two side channels. Vertical focusing relies on wetting of the channel's top and bottom surfaces with the shear fluid. Depending on the specific material system of spinning dope and shear fluid, the channel's surfaces must be coated to realize preferential wetting by the shear fluid. Implementation of new spinning material systems often requires an adaptation of the coating protocol.[17–19] On the other hand, Glass micro-capillaries facilitate centering of the spinning dope jet without tailored surface properties, making a surface coating redundant. However, the glass capillaries need to be manually pulled, cut, and aligned into the shear channel, a task that requires care and skill during assembly.[3,20–22]

Fabrication and assembly are significant limitations in the design of microfluidic spinning devices. Polymerization of the spinning dope requires channel lengths of several millimeters, while the spinneret to create the co-flow of spinning dope and shear fluid has dimensions in the two-digit micrometer range. For perfect centering of the co-flow, placement of the spinneret in the channel requires sub-micron precision. Generally, this challenge is addressed by increasing the spinneret size or through careful manual assembly. Previously, Loelsberg et al. developed a method for precise, rapid prototyping of structures inside microfluidic channels, termed "in-chip direct laser writing (DLW)".[23] Loelsberg et al. fabricated microfluidic molds by DLW, cast those using the established soft-lithography process to produce microfluidic channels, and finally used DLW to write microfluidic spinneret structures "in-chip"; straightaway into the microfluidic channel. They showed the device's functionality by spinning randomly oriented aligned polyacrylonitrile (PAN) fibers.[23] The in-chip DLW fabrication method was applied for the production of microtubes, microfluidic diodes, and microvessels.[24–26]

In microfluidic wet spinning, the concentrically focused pre-polymer jet solidifies with various mechanisms. The most common mechanisms are photopolymerization, ionic or chemical crosslinking, and non-solvent induced phase separation.[16] In photopolymerization, solidification is initiated by irradiation of a photoinitiator. The irradiation, usually with UV light, degrades the photoinitiator into free radicals and initiates a chain reaction with the monomers, leading to large polymer networks. This mechanism is commonly used for hydrogels and artificial polymers, such as polyethylene glycol diacrylate (PEG-DA) or poly(*N*-isopropylacrylamide) (PNIPAm).[27,28] Ionic crosslinking refers to the linking of monomers via multivalent ions. A typical example is the crosslinking of sodium alginate with calcium ions.[19,20] Non-solvent-induced phase separation describes the process of a dissolved monomer jetting into a shear fluid containing a non-solvent. The diffusion-based exchange of solvent and non-solvent leads to an increase of the monomer concentration in the pre-polymer until the critical concentration is reached and the monomer precipitates into a solid polymer. This process is widely applied in the macro-scale, then termed "wet spinning" for the fabrication of porous membranes[29] or fibers,[30,31] and is also common in microfluidic spinning.[32–34] Compared to macro-scale wet spinning, microfluidic spinning allows greater control over the spinning process by applying shear forces during solidification and diffusion-based concentration gradients. Additionally, applying hydrodynamic jetting, microfluidic spinning allows for the production of much thinner fibers.

Fibers intended for cell culture need to be made from biocompatible, non-cytotoxic material to support cell growth. Moreover, despite the small fiber diameter, the fabric needs to be strong enough to allow handling. Inspiration for low-diameter, high-strength fibers can be drawn from nature in the form of silks. These protein fibers are spun on-demand by various insects, and spiders.[35,36] They exhibit extraordinary mechanical strength as well as good biocompatibility and biodegradability. By dissolving and subsequent recasting or spinning, silk can be fabricated in specific shapes and morphologies, tailoring the material for particular applications.[37] Silk can be dissolved by breaking the bonds that, which link the protein chains into a crystal structure, using chaotropic salts (e.g., LiBr, $CaCl_2$) or organic solvents.[38] The potential of both natural and regenerated silk for tissue engineering, especially in the regeneration of muscles and nerves, has been shown in several studies.[39–43] Most frequently, silk is dissolved in aqueous solvents using salts. This process, while avoiding the use of organic solvents, yields structures and fibers with relatively low strength. High-strength silk fibers were produced from silkworm silk dissolved in hexafluoroisopropanol (HFIP) by Ling et al.[44] The impressive mechanical properties of these fibers were achieved through careful design of the material system, based on a thorough understanding of silk chemistry. However, the dry spinning process developed to produced these fibers, by Ling et al. does not allow the production of fibers with more complex geometries. Furthermore, it is limited to spinning dopes based on a volatile solvent. A single, versatile process for producing fibers from diverse material systems with various polymerization mechanisms does still not exist.

In this work, we leverage in-chip DLW to produce microfluidic spinnerets, combining the scalability of conventional microfluidic chips with the versatility of capillary devices. We showcase the function of our spinnerets by producing fibers from polyacrylonitrile and alginate via non-solvent-induced phase separation and ionic crosslinking, respectively. Furthermore, we spun mechanically strong fibers from regenerated silkworm silk with two different cross-section shapes, analyzed their strength depending on their fiber diameter, and tested their biocompatibility through a cell-culture test. By transferring the versatility and adaptability of additive manufacture into the world of microfluidic spinning, this method creates new opportunities for the production of complex fibers tailored towards specific applications in tissue engineering.

© 2021 The Authors. Advanced Healthcare Materials published by Wiley-VCH GmbH

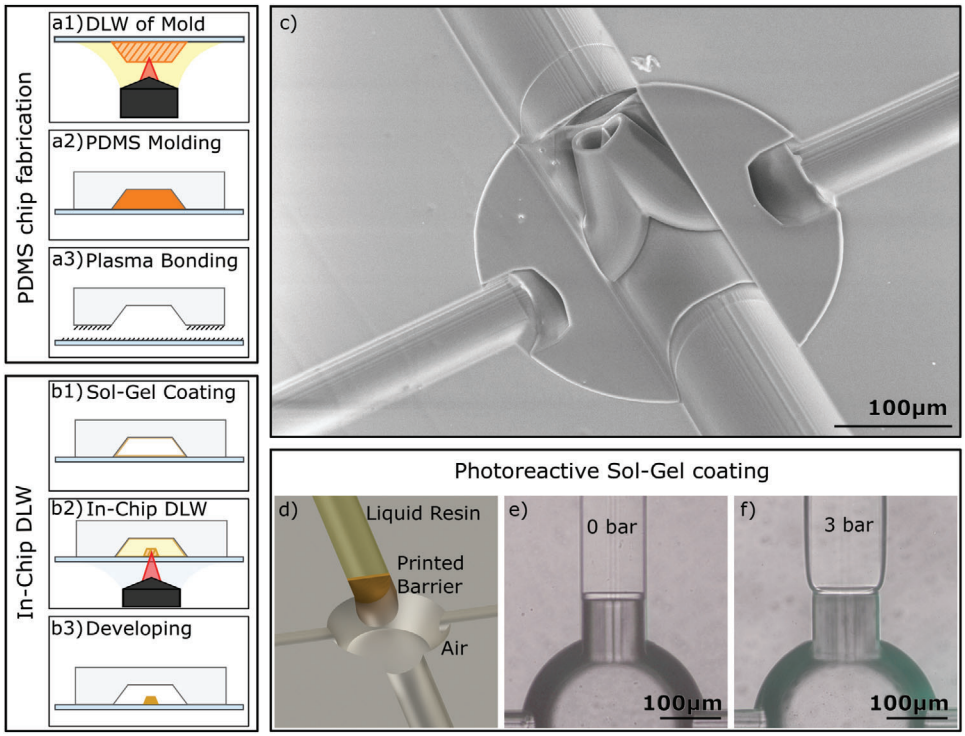

Figure 1. The fabrication process of the microfluidic device consisting of the PDMS chip fabrication (a) and in-chip DLW (b). The PDMS chip fabrication includes direct laser writing of the mold (a1), the PDMS molding (a2), and the plasma bonding of the PDMS chip to a glass slide (a3). The in-chip direct laser writing process includes the sol–gel coating for increased adhesion (b1), the in-chip direct laser writing (b2), and the development of the device (b3). The scanning electron microscopy (SEM) image of the imprinted three-fluid contactor nozzle has a custom 3D-geometry for versatile spinning applications of one and two fluids (c). The photoreactive sol–gel coating (b1) was tested in a burst pressure experiment (d) by applying 0 bar (e) and 3 bar (f) trans-barrier pressure to an imprinted 10 µm thick barrier.

2. Results and Discussion

2.1. Design and Fabrication of Microfluidic Spinnerets

The microfluidic spinnerets are fabricated in a two-step process as shown in **Figure 1**. First, the master mold is printed on a glass slide using DLW in dip-in laser lithography (DILL) mode. The master is molded using PDMS, and the mold is subsequently bonded on a glass slide using oxygen plasma (Figure 1a). Second, the inner surface of the PDMS chip is coated with a photo-reactive sol–gel (see below) to improve the adhesion of the print to the PDMS. Afterward, the channel is filled with the photoresist, and the micronozzle is 3D-printed inside the channel using DLW in oil-immersion mode. Finally, the non-polymerized resin is flushed out of the channel (Figure 1b), and the imprinted nozzle device is ready for the fiber spinning process (Figure 1c). All steps of the production can be parallelized and scaled up without significantly increasing the manual work required. Each of our chips carries six parallel channels, all produced in one printing and one flushing step (see experimental section and Figure S1, Supporting Information).

2.2. Photo-Reactive Sol–Gel Coating for Increased Print Adhesion

The adhesion of the DLW prints inside the PDMS chips is limited by an oxygen inhibition layer on the PDMS surface. In literature, two different methods are suggested to overcome this limitation. Loelsberg et al.[23] overcame the limited adhesion by post-print flooding two sacrificial channels with silane-based epoxy to enclose the in-chip DLW structure for sealing. This attempt adds a laborious manual step to the fabrication process and increases the master mold complexity. The second attempt by Lamont et al.[25] reports an acid-catalyzed sol–gel reaction developed by Beal et al. to coat the PDMS surface with a siliceous layer (APTES) that is not permeable for oxygen.[45] This surface treatment enabled them to print structures with a structure-to-channel sealing and tested the print for withstanding pressure differences up to 0.75 bar. We found that this APTES-based surface modification causes clogging of channels with diameters below 100 µm.

In this study, we present a photo-reactive sol–gel coating, adapted from other PDMS applications.[46] It reduces the oxygen permeability of the PDMS surface and, upon light exposure, the photo-reactive moiety bonds with the resin, resulting in a strong adhesion between the print and the surface. The adhesion and the sealing properties of the structure-to-channel contact were quantified using a burst pressure experiment according to Lamont et al.[25] A barrier with a thickness of 10 µm was printed into a microfluidic channel after treatment with the photo-reactive sol–gel (see Figure 1d). One side of the barrier was developed, such that air is present; the other was pressurized with increasing static pressure until the barrier bursts. The measurements

© 2021 The Authors. Advanced Healthcare Materials published by Wiley-VCH GmbH

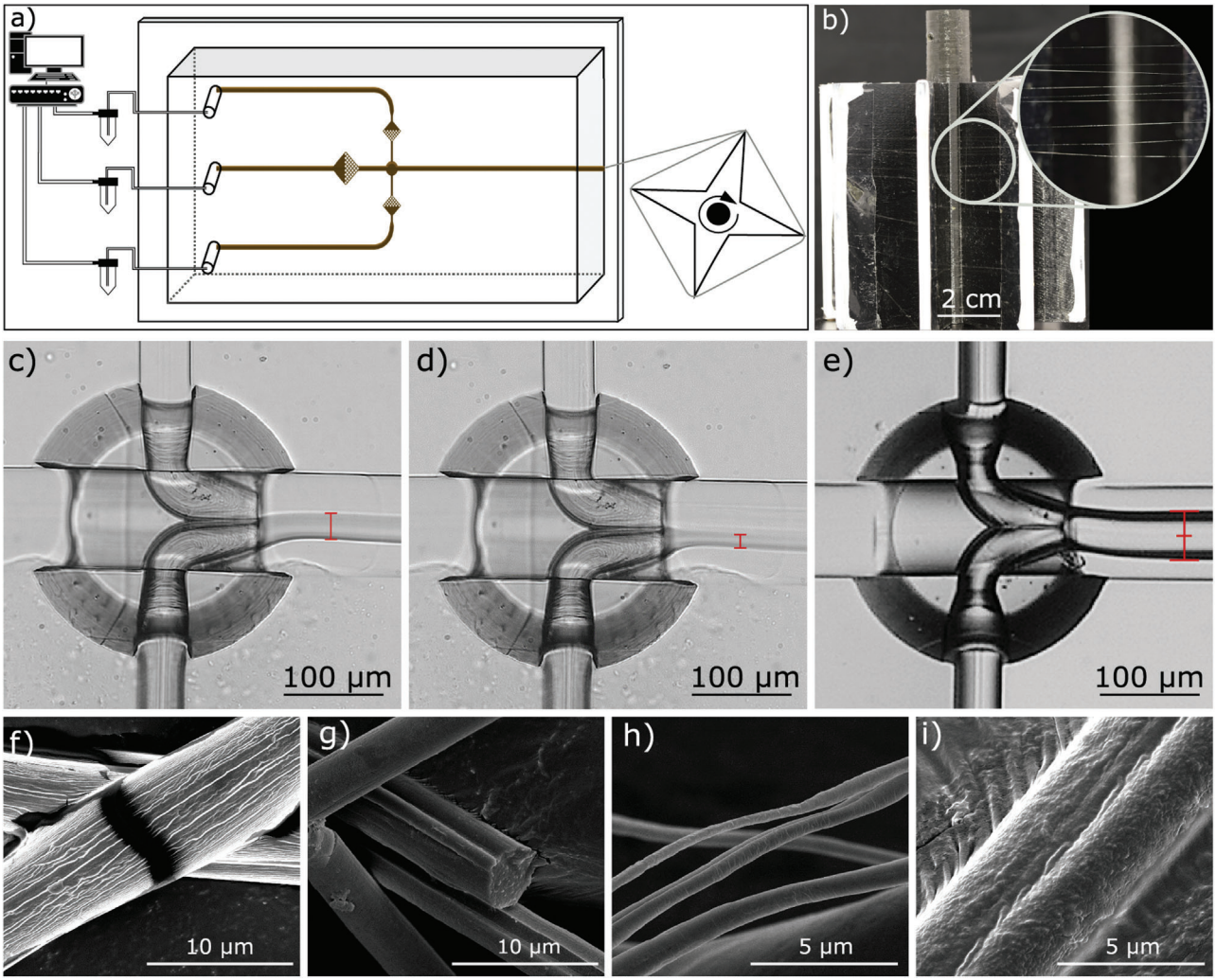

Figure 2. Scheme (a) shows the microfluidic spinning process with digital pressure pumps for the core and shear fluid, the microfluidic PDMS chip with the imprinted nozzle, and the harvesting device. The harvesting device captures the fibers continuously with several meters of length (b). During the spinning process (c, d) the fiber diameter can be adjusted by regulating the shear pressure and flow rate. (c) shows spinning with a shear- and silk-pressure of 160 mbar and 150 mbar, respectively, while (d) shows a flow-focused thinner diameter by applying shear- and silk-pressure of 225 mbar and 150 mbar. The two parallel nozzle orifices enable spinning of single (c,d) or double (e) fibers by co-extrusion of spinning dope through both nozzle orifices. FESEM images of the fibers with different material systems including alginate fibers (f), polyacrylonitrile fibers (g) and regenerated *B. mori* silk fibers as a single fiber (h) and a co-extruded double-fiber (i)

(Figure 1e,f) reveal that a 10 µm thick barrier can withstand pressures up to 3 bar without any noticeable burst or leakage. At this pressure, the surrounding soft PDMS channel shows pressure-induced swelling.

The photo-reactive sol–gel coating[46] applied in our work combines the advantages of the two methods presented in literature,[23,25] a strong and liquid-tight sealing of DLW-printed structures with PDMS, as well as simple applicability in the laboratory.

2.3. Production of Fibers with Different Materials and Precise Diameter Control

The microfluidic setup for spinning microfibers consists of fluid pumps, a microfluidic PDMS chip and a harvesting device (**Figure 2**a). The spinning dope and shear fluid are each pumped by a digital constant pressure pump and flushed into the microfluidic chip with the nozzle in the center part (see Figure 1c). At the nozzle tip, the spinning dope is injected into the center of the shear fluid without contacting the outlet channel wall. Therefore, surface modifications in the outlet channel are not necessary. The spinning dope solidifies in the outlet channel of the device, and the fiber is harvested by spooling on a digitally controlled harvesting coil (Figure 2b).

We chose three exemplary fiber materials to show the versatility of possible solidification mechanisms with the in-chip DLW nozzle. We spun ionic crosslinked alginate fibers (Figure 2f), polymeric precipitated PAN fibers (Figure 2g), and protein precipitated regenerated *B. mori* silk fibers (Figure 2h,i). To enable a stable spinning process without nozzle blocking, we tuned the

© 2021 The Authors. Advanced Healthcare Materials published by Wiley-VCH GmbH

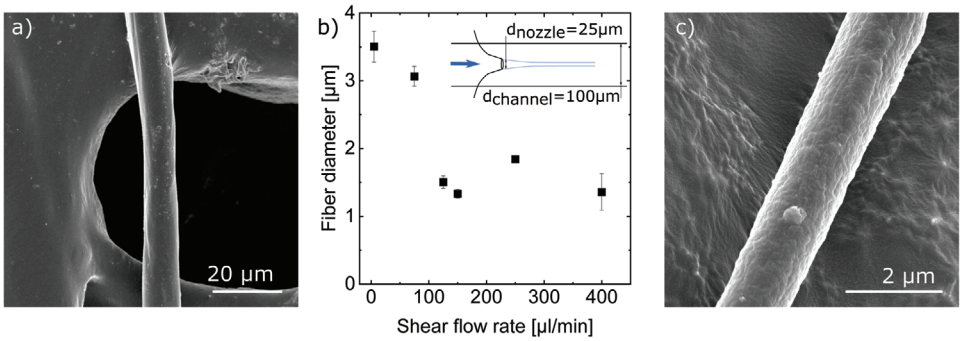

Figure 3. Diameter control of harvested silk fibers ranging from more than 10 µm (a) to approximately 1.5 µm (c). The fiber diameter is controlled by varying the shear flow rate (b). The core flow rate was constant at 5 µL/min and the shear flow rate was adjusted from 5 µL/min to 400 µL/min. The microfluidic device used had a channel width of 100 µm and a nozzle diameter of 25 µm. Each data point was averaged from 10 diameter measurements at different fiber positions of two fibers from the same fiber spinning batch. Additional images of the fibers can be found in Figure S2, Supporting Information.

solidification kinetics by changing the salt concentration and the non-solvent concentration of the shear fluid for the alginate fibers and PAN and silk fibers, respectively (see Section 4).

The alginate fibers and the PAN fibers with diameters smaller than 10 µm show poor mechanical properties, such that the fibers tend to break and to elongate during fiber harvesting and processing. For the mechanically strong regenerated silk, fibers with diameters down to 1.5 µm can be harvested continuously on the spooling device and processed for stress–strain measurement. Although smaller fibers down to 0.8 µm (see Figure 2h) can be produced, single fiber harvesting and processing is challenging. Accordingly, the alginate fiber (Figure 2f), the PAN fiber (Figure 2g) and the silk fiber with diameters smaller than 1.5 µm (Figure 2h) were only spun in solution and not harvested. The larger morphology of different fibers including micrographs with 50 µm scale bar can be found in Figure S2, Supporting Information.

For the silk fiber, we used PEG (300 Da) as inert shear fluid to decelerate precipitation and to increase the shear fluid's viscosity and the spinning process's stability. Using this viscosity adaption, we were able to produce and harvest several meters of silk fibers in a continuous process. By increasing the shear flow rate, the silk solution is hydrodynamically accelerated in the outlet channel (Figure 2c,d), controlling the fiber diameter from 1.5 µm (**Figure 3**c) to 10 µm (Figure 3a). The final fiber diameter depends on the applied flow rates and the geometric parameters of the microfluidic device, that is, channel size and nozzle diameter. Studying the influence of the shear flow rate at constant core flow rate in a device with channel width of 100 µm and nozzle diameter of 25 µm, we received a minimum fiber diameter of approximately 1.5 µm for a core fluid of 5 µL/min and a shear fluid of 125 µL/min. Higher shear fluid rates did not decrease the fibers diameter further (Figure 3b). Applying smaller shear flow rates than 5 µL/min results in larger fibers (**Figure 4**), while shear flow rates smaller than the core flow rate hold the risk of the fiber blocking the outlet channel. Decreasing the core flow rate decreases the fiber size (Figure 2h), but hinders single fiber harvesting.

Finally, we fabricated single fibers and co-extruded double fibers by flushing the dope solution through one (Figure 2c,d) or both (Figure 2e) nozzle orifices in the imprinted structure. The co-extruded fibers show an 8-shaped cross-section (Figure 2i), similar to the natural *B. mori* silk.[47] Though, the artificial fibers with diameters down to 1 µm are significantly smaller than the natural silk fibers, which have diameters of 10–30 µm.[48]

To our knowledge, there are no microfluidic wet-spun fibers with diameters as small as 1.5 µm reported yet. Other microfluidic nozzle-less wet spinning approaches need a phase boundary to center the core fluid in the channel. This phase boundary destabilizes the jet at high shear velocities and small diameters, promoting droplet formation instead of jetting.[49] Other microcapillary devices are challenging to assemble and center inside microfluidic channels with channel sizes as small as 50–100 µm, limiting the diameter of the fiber. The in-chip direct laser written nozzle combines the microfluidic preciseness with the centered nozzle, such that this technology enables the fabrication of smaller fibers with different geometries.

2.4. Tensile Strength of Silk Fibers

For tissue engineering, protein-based silk is advantageous due to its biocompatibility and its tensile strength. We analyzed the tensile strength of the microfluidic spun silk fibers by measuring the tensile force and strain using a self-built tensile test setup. By analyzing the diameter of the fibers using field emission scanning electron microscopy (FESEM) images, we were able to estimate the stress–strain diagram (Figure 4a), the tensile strength at the breaking point (Figure 4b), and the Young's modulus (**Table 1**). The measurement accuracy and the size of the error bars confirms other literature data using microfluidically spun regenerated silk fibers.[44,50]

Comparing these stress–strain measurements with literature data, we find two conspicuous phenomena. First, the average breaking stress and Young's modulus of our fibers seems to be significantly smaller than reported fibers.[44,51,52] Most spinning processes include an additional post-spin stretching process step to support the formation of beta-sheets and significantly increase strength and extensibility.[52,53] Comparing our data with

© 2021 The Authors. Advanced Healthcare Materials published by Wiley-VCH GmbH

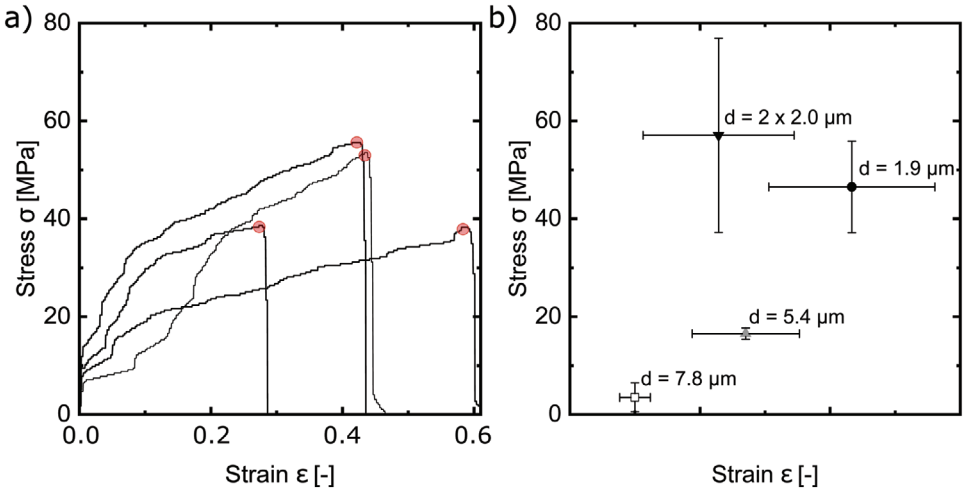

Figure 4. a) Exemplary stress–strain diagram of the 1.9 µm regenerated silk fiber measurements with labeled breaking points. b) Breaking points for regenerated silk fibers at different diameters. The silk was dissolved in HFIP and precipitated in 68 vol% EtOH in PEG (300 Da). 2 × 2.0 µm fiber is a co-extruded fiber, using both nozzles as shown in Figure 2e. Fiber diameters were measured by FESEM images. The sample size of the 7.8 µm, 5.4 µm, 1.9 µm, and 2 × 2.0 µm samples are 4, 2, 4, and 10, respectively. Comparing the breaking stress of the 7.8 µm and 5.4 µm fiber gives a significant *p* value of 0.003. The breaking stress comparison of the 1.9 µm or 2 × 2.0 µm with the 5.4 µm fiber results in a significant *p* value of 0.007 or 0.0001, respectively.

Table 1. Mechanical properties including the Young's modulus and the breaking point stress and strain of HFIP dissolved silk fibers.

Diameter [µm]	Nr. of samples (–)	Young's modulus [MPa]	Breaking strain (–)	Breaking stress [MPa]
7.8	4	28.3 ± 24.8	0.10 ± 0.03	3.5 ± 3.4
5.4	2	244.0 ± 55.7	0.27 ± 0.08	16.5 ± 1.2
1.9	4	222.4 ± 66.5	0.43 ± 0.13	46.5 ± 9.3
2 × 2.0	10	1052.5 ± 419.8	0.23 ± 0.12	57.1 ± 19.9

They were spun with a shear fluid consisting of 68 vol% ethanol in PEG (300 Da) as plotted in Figure 4b. The 2 × 2.0 is a co-extruded fiber with two cores as shown in Figure 2e,i.

the as-spun mechanical properties, we result in similar breaking ranges.[32,44,52]

Second, our data reveal significantly higher strength, the smaller the diameter. Based on Griffith's criterion on fracture mechanics, it is known that smaller fiber diameters increase toughness.[54] This effect was studied for other silk fibers by Porter et al.[55] They state, that decreasing diameters promote the high toughness of spider drag-line silk (d = 5 µm) compared to silkworm silk (d = 25 µm).[55] Additionally to Griffith's criterion, for silk fibers, the nano-scale composition of the material, which is adjusted in the elsewhere established post-spin stretching process,[52,53] has a significant influence on the mechanical properties.[32,56] In our wet-spinning process, we control the diameter of the fiber by adjusting the shear flow rate and stretching the dope solution during the precipitation process by hydrodynamic shear forces. This hydrodynamic stretching during polymerization is similar to the post-spin stretching process, which modifies the nano-structure. Stretching increases beta-sheet formation during fiber solidification and would explain the increased breaking energies, the smaller the diameter. Accordingly, the microfluidic wet spinning process combines precipitation and post-spin stretching in a one-step process.

The co-extruded double fiber (2 × 2.0 µm) with a 8-shaped cross section (see Figure 2i) shows a similar breaking stress, but an increased Young's modulus (see Table 1) compared to the 1.9 µm fiber. Even though the shear stress and the consequent internal morphology of both fibers are similar, the raising Young's modulus might result from the increased surface to cross-section ratio. Additionally, the increased cross-section size lowers the probability of failure and increases the average stability. Accordingly, the spinning velocities and the fiber shape tailor the mechanical properties, including breaking stress and the Young's modulus.

2.5. Cell Culture

The mechanical properties are of major importance considering the tissue engineering applications of the fibers. Cell adhesion and stem cell differentiation depend on mechanical properties, such as the Young's modulus. As cells adhere to the fiber's surface, the surface-to-volume ratio, which increases as the the fiber diameter decreases, is a critical parameter to enhance cell density in a fiber bundle. That way, smaller fiber diameters reduce the amount of implanted foreign material. As a first step toward using the silk-fibers as tissue material, we cultivated human epithelial colorectal adenocarcinoma (CaCo2) cells on regenerated silk fibers. Before cultivation, the fibers were washed to remove any residual solvent.the fibers. We visualized cell morphology after three days of cultivation using fluorescent microscopy. **Figure 5** shows cells enclosing the fibers, where cells form clusters in distinct areas (Figure 5b), which are interconnected by actin filaments. This study is a first step to show that silk fibers fabricated by our process are suitable for tissue engineering applications.This study confirms the bio-compatibility of the silk fibers fabricated by our process. This promising result

© 2021 The Authors. Advanced Healthcare Materials published by Wiley-VCH GmbH

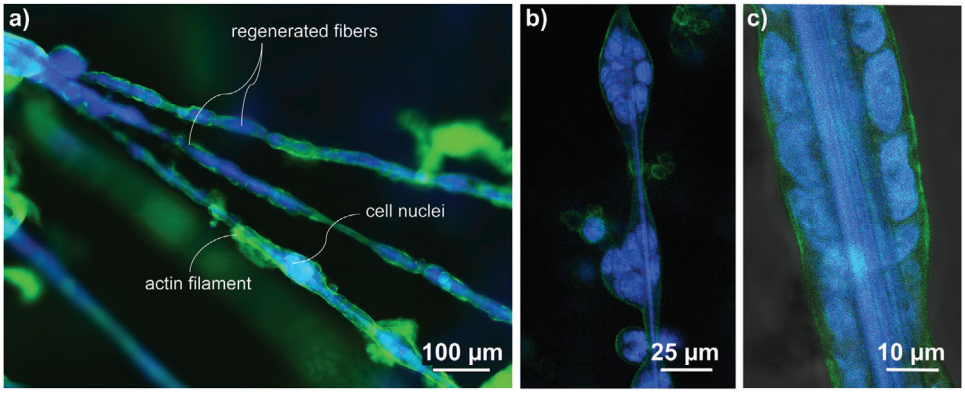

Figure 5. Fluorescent micrograph (a) and confocal images (b,c) of CaCo2 cells cultured on regenerated silk fibers with actin filament stained by phalloidin (green) and nuclei by DAPI (blue). The regenerated silk fibers occurs in blue in the center of the cells.

encourages to evaluate further the influence of the material properties, shape, and size on its performance as a tissue engineering material.

3. Conclusion

This paper presents an in-chip DLW fabrication of a versatile microfluidic fiber spinning system capable of synthesizing micron-scale fibers of various materials with different cross-section geometries. For protein-based silk fibers, we control the Young's modulus and the breaking stress by process parameters and show suitability for cell culture, indicating biocompatibility of the fibers for different tissue engineering applications. The integration of nano-scale DLW into microfluidic applications replaces manual lab methods using micro-capillaries by automated 3D-printing and enables improved accuracy, better resolution, and complex nozzle and fiber geometries. Future studies will be dedicated to transferring the methodological potential of the process, such as composite multi-material fibers and complex fiber geometries, toward sophisticated applications in tissue engineering.

4. Experimental Section

Production of Microfluidic Chips: Production of the spinnerets with in-chip DLW is a two-step process. First is the production of microfluidic chips, followed by the in-chip lithography of the spinneret.

The microfluidic chips are produced from polydimethylsiloxane via replica molding. The master mold with the negative of the channel layout was produced using a two-photon lithography printer (Photonic GT, Nanoscribe GmbH, Karlsruhe, Germany). Standard microscopy slides (76 × 26 mm) were used as DILL substrates for the microfluidic masters, ensuring standardization and compatibility with existing equipment, such as, for example, microscopes. Liquid PDMS-elastomer (ratio 10:1) is poured on the master, degassed in a vacuum to remove trapped air for 2 h, and crosslinked in an oven at 60 °C for 3 h. After crosslinking, the cured PDMS is peeled off the master and plasma bonded to a microscopy coverslip (150 µm thickness) to seal off the channels.

Sol–Gel Activation: The protocol for treating the channel surfaces is adopted from Abate et al.[46] The solution was prepared as described. A drop of the solution is placed on the outlet of the channel network and capillary forces pull the liquid inside the channels, such that it wets all surfaces of the channel network. The solution is left in the channel for 1 min before displacing it by flushing air through the shear inlet via a syringe.

In-Chip Fabrication: After sol–gel activation of the PDMS surfaces, a liquid negative-tone photoresist (IP-S, Nanoscribe GmbH, Karlsruhe, Germany) is flushed into the channel using a syringe. The chip is placed in the two-photon lithography printer (Photonic GT, Nanoscribe GmbH, Germany). The printer is set up for printing in oil immersion mode with the 25× objective. Marker structures on the microfluidic chip are manually located to determine the printing coordinates of the spinnerets. Printing parameters and trajectories are supplied in a .gwl file, Nanoscribe's proprietary programming language. Printing time per nozzle was about 30 min. Multiple prints can be done inline, limited only by the available space in the Nanoscribe printer. After the print, the chip is developed by removing uncured resist from the channel by connecting the outlet to a vacuum source, while all inlets are connected to reservoirs containing 1 mL acetonitrile solvent. As soon as all acetonitrile containers are emptied, the chips are ready for use. Multiple channels can be developed in parallel.

Evaluation of the Reactive Seal: The reactive seal using the sol–gel activation was evaluated using a burst pressure test adapted from.[25] A channel was closed off with an in-chip printed 10 µm thick barrier. One side of the barrier was developed, so that the barrier was covered on one side with photoresist and air on the other side. The side with photoresist was connected to a pressure reservoir using PE tubes (VWR - ID 0.38mm) glued into the punched inlet holes. The reservoir connected to the resist filled chamber was pressurized using a piezo controlled constant pressure system (OB1 MK3+, Elveflow, France). The pressure was increased in steps of 10 mbar/min. The barrier was visually observed through an inverse light microscope (Leica, Germany). Upon reach of a critical pressure, collapse of the barrier and liquid flow were clearly visible. This critical pressure was recorded as the burst pressure.

Spinning Dope Preparation: The alginate solution was prepared according to Shin et al.[20] Sodium alginate powder (Sigma-Aldrich Chemie GmbH, Munich, Germany) was dissolved in deionized water to a concentration of 4 wt% under stirring for 2 h at room temperature. The PAN solution was produced as described by Loelsberg et al.[23] PAN (Sigma-Aldrich Chemie GmbH, Munich, Germany) was dissolved in dimethylsulfoxide (Sigma-Aldrich Chemie GmbH, Munich, Germany) to a concentration of 2 wt%. The silk spinning dope was prepared following a procedure developed by Ling et al.[44] *B. mori* silk cocoons (Amazon) were degummed by boiling twice in an aqueous solution of 0.5 wt% Na_2CO_3 for 30 min. In between, the silk was rinsed extensively with distilled water. The silk was dried at room temperature, cut into small pieces and immersed in pure hexafluoroisopropanol (HFIP, Sigma Aldrich GmbH, Munich, Germany) at a weight ratio of 1:50. The solution was incubated in airtight containers at 60 °C for 15 days in a fume hood.

© 2021 The Authors. Advanced Healthcare Materials published by Wiley-VCH GmbH

Microfluidic Spinning: The fibers were spun using the microfluidic device with the in-chip DLW printed nozzle. The shear solutions of the alginate, PAN and silk solution were aqueous 784 mM $CaCl_2$ solution, 35 wt% deionized water in DMSO, and 68 vol% ethanol in polyethylene glycol (300 Da) (PEG), respectively. Spinning dope and shear fluid were filled into microfluidic reservoirs and connected to the microfluidic chip via polyethylene tubing. Pressure-driven flow control was realized with a digital constant pressure system (OB1 MK3+, Elveflow, France). The spinning process was initiated by increasing the shear fluid pressure until the channel was filled. The dope channel pressure was increased in parallel to avoid flooding the dope channel with shear fluid. The shear fluid pressure is incrementally increased to 150 mbar. When the operating shear flow pressure is reached, the dope pressure is slowly increased until the air trapped inside the channel and tubing starts flowing through the nozzle into the shear flow. After removal of the residual air, the spinning dope flows through the nozzle to form a co-flow. The spinning process and fiber formation was observed with an inverse microscope. Manipulation of shear and dope pressures allows adjustment of the fiber diameter. The experiments on the relationship between the fiber diameter and the shear flow rate (Figure 3) were performed using syringe pumps (Harvard PHD Ultra) instead of the pressure driven pumps. The experimental procedure was adapted from the pressure-driven set up. The fiber was picked up with tweezers and placed on a custom build rotating spindle for collection. The rotational speed of the spindle can be controlled to adjust the fiber's collection rate.

Tensile Testing: Tensile tests were done on a custom-built setup adapted from the setup used in Joel et al.[57] It consists of a precision scale (JB1603/C-FACT, Mettler Toledo, Columbus, Ohio, USA) and a linear micromanipulator arm (MM 33; Märzhauser Wetzlar GmbH & Co. KG, Wetzlar, Germany) that is automatically moving upwards using a connected stepper motor (17HS13-0404S1; Stepperonline, Greater London, UK). Fibers for tensile tests were directly collected onto c-shaped cardboard holders to avoid stretching during transfer. The legs of the cardboard holder had a distance of 10 mm to set the initial length of the fibers. The cardboard holder was fixed with clamps to the linear arm and the scale. The cardboard was cut, leaving only the fiber as a connection between the scale and the linear arm. The fiber was stretched to failure by moving the linear arm upwards at a speed of 0.2 mm s^{-1}. A self-written python script recorded extension and scale readings.

Cell Culture: Human epithelial colorectal adenocarcinoma (CaCo2) cells were seeded on the artificial spun silk fibers and cultivated for 3 days at 37 °C and 5% CO_2 (Heraeus, Hanau, Germany). Prior, the fibers were incubated at 37 °C for 24 h with 50 µg mL^{-1} collagen I and washed with phosphate-buffered saline (PBS, Lonza Group AG, Basel, Switzerland) afterward. Therefore, the artificial fibers were stretched over a cover glass slide (18 × 18 mm, Carl Roth GmbH + Co. KG, Karlsruhe, Germany) and glued (UHU Holding GmbH, B ühl, Germany) at the edges to fix them on the glass. The culture medium used for CaCo2 cells consisted of a minimum essential medium eagle (EMEM, Sigma-Aldrich, St. Louis, Missouri, USA) as a basis and 10 vol% fetal bovine serum (FBS, biowest, Nuaillé, France), 2 mM L-glutamin (Sigma-Aldrich, St. Louis, Missouri, USA), 1 vol% of a hundredfold non-essential amino acids solution (NEAA, Sigma-Aldrich, St. Louis, Missouri, USA) and 50 U/mL penstrep (Thermo Fisher Scientific Inc., Waltham, MA, USA) as supplements. The actin filament and the nuclei were stained with phalloidin (abcam, Cambridge, UK) and 4′,6′-diamidino-2-phenylindole (DAPI, AppliChem GmbH, Darmstadt, Germany), respectively. Fluorescent microtome (ApoTome, Carl Zeiss AG, Oberkochen, Germany) and confocal (SP8 Lightning, Leica Microsystems, Wetzlar, Germany) images show the fluorescently stained cells.

Statistical Analysis: The tensile strength of silk fiber data was statistically analyzed using the following processing steps. As pre-processing, the breaking points were selected manually from the measured data as exemplary shown in Figure 4a. The Young's modulus was determined by fitting a linear function to the elastic region of the measured data. The data presented in Table 1 shows no. of samples, the mean value, and the standard deviation of the sample. The p values were calculated by two-sided testing using a t-test. The data was processed using Microsoft Excel 2016.

Supporting Information

Supporting Information is available from the Wiley Online Library or from the author.

Acknowledgements

A.L. and M.G. contributed equally to this work. This work was funded by the Deutsche Forschungsgemeinschaft (DFG, German Research Foundation) - 436799631. Furthermore, this work was supported by the European Union's Horizon 2020 research and innovation program within the project "BioComb4Nanofibers" (Grant Agreement No. 862016) and the Excellence Initiative of the German federal and state governments by the project "Biospin". M.W. acknowledges DFG funding through the Gottfried Wilhelm Leibniz Award 2019 (WE 4678/12-1). Part of the work was performed at the Center for Chemical Polymer Technology CPT, which is supported by the EU and the federal state of North Rhine-Westphalia (Grant No. EFRE 30 00 883 02). The authors thank Karin Faensen for capturing beautiful FE-SEM images of non-visible samples, Patrick Bongartz for fruitful discussions, and Margret Weißbach for early stage lab support.

Open access funding enabled and organized by Projekt DEAL.

Conflict of Interest

The authors declare no conflict of interest.

Data Availability Statement

The data that support the findings of this study are available from the corresponding author upon reasonable request.

Keywords

2-photon lithography, additive manufacturing, material properties, tissue engineering

Received: May 7, 2021
Revised: June 17, 2021
Published online: July 31, 2021

[1] L. Papadimitriou, P. Manganas, A. Ranella, E. Stratakis, *Mater. Today Bio* **2020**, *6*, 100043.
[2] S. C. Neves, L. S. Moreira Teixeira, L. Moroni, R. L. Reis, C. A. Van Blitterswijk, N. M. Alves, M. Karperien, J. F. Mano, *Biomaterials* **2011**, *32*, 1068.
[3] C. M. Hwang, A. Khademhosseini, Y. Park, K. Sun, S.-H. Lee, *Langmuir* **2008**, *24*, 6845.
[4] A. Tamayol, M. Akbari, N. Annabi, A. Paul, A. Khademhosseini, D. Juncker, *Biotechnol. Adv.* **2013**, *31*, 669.
[5] C. Licht, J. C. Rose, A. O. Anarkoli, D. Blondel, M. Roccio, T. Haraszti, D. B. Gehlen, J. A. Hubbell, M. P. Lutolf, L. De Laporte, *Biomacromolecules* **2019**, *20*, 4075.
[6] M. Yamada, S. Sugaya, Y. Naganuma, M. Seki, *Soft Matter* **2012**, *8*, 3122.
[7] J. C. Rose, D. B. Gehlen, T. Haraszti, J. Köhler, C. J. Licht, L. De Laporte, *Biomaterials* **2018**, *163*, 128.
[8] F. Sharifi, B. B. Patel, A. K. Dzuilko, R. Montazami, D. S. Sakaguchi, N. Hashemi, *Biomacromolecules* **2016**, *17*, 3287.
[9] A. Omidinia-Anarkoli, S. Boesveld, U. Tuvshindorj, J. C. Rose, T. Haraszti, L. De Laporte, *Small* **2017**, *13*, 1702207.

© 2021 The Authors. Advanced Healthcare Materials published by Wiley-VCH GmbH

[10] E. Kang, Y. Y. Choi, S.-K. Chae, J.-H. Moon, J.-Y. Chang, S.-H. Lee, *Adv. Mater.* **2012**, *24*, 4271.
[11] M. Darnell, A. O'Neil, A. Mao, L. Gu, L. L. Rubin, D. J. Mooney, *Proc. Natl. Acad. Sci. USA* **2018**, *115*, E8368.
[12] Y. Jun, E. Kang, S. Chae, S.-H. Lee, *Lab Chip* **2014**, *14*, 2145.
[13] Q. P. Pham, U. Sharma, A. G. Mikos, *Biomacromolecules* **2006**, *7*, 2796.
[14] L. Persano, A. Camposeo, C. Tekmen, D. Pisignano, *Macromol. Mater. Eng.* **2013**, *298*, 504.
[15] B.-M. Min, G. Lee, S. H. Kim, Y. S. Nam, T. S. Lee, W. H. Park, *Biomaterials* **2004**, *25*, 1289.
[16] X.-Y. Du, Q. Li, G. Wu, S. Chen, *Adv. Mater.* **2019**, *31*, 1903733.
[17] J. H. Jung, C. H. Choi, S. Chung, Y. M. Chung, C. S. Lee, *Lab Chip* **2009**, *9*, 2596.
[18] Q. Huang, Y. Li, L. Fan, J. H. Xin, H. Yu, D. Ye, *Lab Chip* **2020**, *20*, 3158.
[19] E. Kang, S.-J. Shin, K. H. Lee, S.-H. Lee, *Lab Chip* **2010**, *10*, 1856.
[20] S.-J. Shin, J.-Y. Park, J.-Y. Lee, H. Park, Y.-D. Park, K.-B. Lee, C.-M. Whang, S.-H. Lee, *Langmuir* **2007**, *23*, 9104.
[21] Y. Yu, L. Shang, J. Guo, J. Wang, Y. Zhao, *Nat. Protoc.* **2018**, *13*, 2557.
[22] Y. Yu, F. Fu, L. Shang, Y. Cheng, Z. Gu, Y. Zhao, *Adv. Mater.* **2017**, *29*, 18.
[23] J. Lölsberg, J. Linkhorst, A. Cinar, A. Jans, A. J. C. Kuehne, M. Wessling, *Lab Chip* **2018**, *18*, 1341.
[24] J. Lölsberg, A. Cinar, D. Felder, G. Linz, S. Djeljadini, M. Wessling, *Small* **2019**, *15*, 1.
[25] A. C. Lamont, A. T. Alsharhan, R. D. Sochol, *Sci. Rep.* **2019**, *9*, 394.
[26] A. T. Alsharhan, R. Acevedo, R. Warren, R. D. Sochol, *Lab Chip* **2019**, *19*, 2799.
[27] H. J. M. Wolff, J. Linkhorst, T. Göttlich, J. Savinsky, A. J. D. Krüger, L. de Laporte, M. Wessling, *Lab Chip* **2020**, *20*, 285.
[28] A. J. D. Krüger, O. Bakirman, L. P. B. Guerzoni, A. Jans, D. B. Gehlen, D. Rommel, T. Haraszti, A. J. C. Kuehne, L. De Laporte, *Adv. Mater.* **2019**, *31*, 1903668.
[29] M. Mulder, J. Mulder, *Basic Principles of Membrane Technology*, Springer Science & Business Media, New York **1996**.
[30] Q. Cui, D. J. Bell, S. B. Rauer, M. Wessling, *Adv. Mater. Interfaces* **2020**, *7*, 2000849.
[31] M. Desorme, A. Montembault, T. Tamet, P. Maleysson, T. Bouet, L. David, *J. Appl. Polym. Sci.* **2019**, *136*, 47130.
[32] M. E. Kinahan, E. Filippidi, S. Köster, X. Hu, H. M. Evans, T. Pfohl, D. L. Kaplan, J. Wong, *Biomacromolecules* **2011**, *12*, 1504.
[33] S. Li, Y. Hang, Z. Ding, Q. Lu, G. Lu, H. Chen, D. L. Kaplan, *ACS Biomater. Sci. Eng.* **2020**, *6*, 2847.
[34] Q. Peng, Y. Zhang, L. Lu, H. Shao, K. Qin, X. Hu, X. Xia, *Sci. Rep.* **2016**, *6*, 1.
[35] F. Vollrath, D. Porter, C. Holland, *MRS Bull.* **2013**, *38*, 73.
[36] J. G. Hardy, L. M. Römer, T. R. Scheibel, *Polymer* **2008**, *49*, 4309.
[37] A. Koeppel, C. Holland, *ACS Biomater. Sci. Eng.* **2017**, *3*, 226.
[38] R. L. Lock Process for Making Silk Fibroin Fibers 1993.
[39] A. M. Hopkins, L. De Laporte, F. Tortelli, E. Spedden, C. Staii, T. J. Atherton, J. A. Hubbell, D. L. Kaplan, *Adv. Funct. Mater.* **2013**, *23*, 5140.
[40] V. Benfenati, K. Stahl, C. Gomis-Perez, S. Toffanin, A. Sagnella, R. Torp, D. L. Kaplan, G. Ruani, F. G. Omenetto, R. Zamboni, M. Muccini, *Adv. Funct. Mater.* **2012**, *22*, 1871.
[41] V. J. Neubauer, A. Döbl, T. Scheibel, *Materials* **2021**, *14*, 674.
[42] H. J. Kim, U.-J. Kim, G. Vunjak-Novakovic, B.-H. Min, D. L. Kaplan, *Biomaterials* **2005**, *26*, 4442.
[43] C. Lei, H. Zhu, J. Li, J. Li, X. Feng, J. Chen, *Polym. Eng. Sci.* **2015**, *55*, 907.
[44] S. Ling, Z. Qin, C. Li, W. Huang, D. L. Kaplan, M. J. Buehler, *Nat. Commun.* **2017**, *8*, 1.
[45] J. H. L. Beal, A. Bubendorfer, T. Kemmitt, I. Hoek, W. Mike Arnold, *Biomicrofluidics* **2012**, *6*, 036503.
[46] A. R. Abate, D. Lee, T. Do, C. Holtze, D. A. Weitz, *Lab Chip* **2008**, *8*, 516.
[47] V. Benfenati, K. Stahl, C. Gomis-Perez, S. Toffanin, A. Sagnella, R. Torp, D. L. Kaplan, G. Ruani, F. G. Omenetto, R. Zamboni, M. Muccini, *Adv. Funct. Mater.* **2012**, *22*, 1871.
[48] M. Tsukada, M. Obo, H. Kato, G. Freddi, F. Zanetti, *J. Appl. Polym. Sci.* **1996**, *60*, 1619.
[49] A. R. Abate, A. Poitzsch, Y. Hwang, J. Lee, J. Czerwinska, D. A. Weitz, *Phys. Rev. E* **2009**, *80*, 26310.
[50] Z. Li, J. Dong, J. Huang, T. Guo, S. Wang, X. Zhao, Q. Zhang, *Macromol. Res.* **2020**, *28*, 1.
[51] C. Zhao, J. Yao, H. Masuda, R. Kishore, T. Asakura, *Biopolymers* **2003**, *69*, 253.
[52] G. Fang, Y. Huang, Y. Tang, Z. Qi, J. Yao, Z. Shao, X. Chen, *ACS Biomater. Sci. Eng.* **2016**, *2*, 1992.
[53] K. Yazawa, A. D. Malay, N. Ifuku, T. Ishii, H. Masunaga, T. Hikima, K. Numata, *Biomacromolecules* **2018**, *19*, 2227.
[54] A. A. Griffith, *Philos. Trans. Royal Soc. London. Series A* **1921**, *221*, 163.
[55] D. Porter, J. Guan, F. Vollrath, *Adv. Mater.* **2013**, *25*, 1275.
[56] H. Gao, B. Ji, I. L. Jäger, E. Arzt, P. Fratzl, *Proc. Natl Acad. Sci.* **2003**, *100*, 5597.
[57] A.-C. Joel, M. Meyer, J. Heitz, A. Heiss, D. Park, H. Adamova, W. Baumgartner, *ACS Appl. Nano Mater.* **2020**, *3*, 3395.

© 2021 The Authors. Advanced Healthcare Materials published by Wiley-VCH GmbH